The Astrophysical Journal Letters, 869:L44 (13pp), 2018 December 20 https://doi.org/10.3847/2041-8213/aaf746

The Disk Substructures at High Angular Resolution Project (DSHARP). IV. Characterizing Substructures and Interactions in Disks around Multiple Star Systems

Nicolás T. Kurtovic[1], Laura M. Pérez[1], Myriam Benisty[1,2,3], Zhaohuan Zhu[4], Shangjia Zhang[4], Jane Huang[5], Sean M. Andrews[5], Cornelis P. Dullemond[6], Andrea Isella[7], Xue-Ning Bai[8], John M. Carpenter[9], Viviana V. Guzmán[9,10], Luca Ricci[11], and David J. Wilner[5]

[1] Departamento de Astronomía, Universidad de Chile, Camino El Observatorio 1515, Las Condes, Santiago, Chile; nicokurtovic@gmail.com
[2] Unidad Mixta Internacional Franco-Chilena de Astronomía, CNRS/INSU UMI 3386, France
[3] Univ. Grenoble Alpes, CNRS, IPAG, F-38000 Grenoble, France
[4] Department of Physics and Astronomy, University of Nevada, Las Vegas, 4505 S. Maryland Parkway, Las Vegas, NV 89154, USA
[5] Harvard-Smithsonian Center for Astrophysics, 60 Garden Street, Cambridge, MA 02138, USA
[6] Zentrum fr¨ Astronomie, Heidelberg University, Albert Ueberle Str. 2, D-69120 Heidelberg, Germany
[7] Department of Physics and Astronomy, Rice University 6100 Main Street, MS-108, Houston, TX 77005, USA
[8] Institute for Advanced Study and Tsinghua Center for Astrophysics, Tsinghua University, Beijing 100084, People's Republic of China
[9] Joint ALMA Observatory, Avenida Alonso de Córdova 3107, Vitacura, Santiago, Chile
[10] Instituto de Astrofísica, Pontificia Universidad Católica de Chile, Av. Vicuña Mackenna 4860, 7820436 Macul, Santiago, Chile
[11] Department of Physics and Astronomy, California State University Northridge, 18111 Nordhoff Street, Northridge, CA 91130, USA
Received 2018 October 23; revised 2018 November 26; accepted 2018 December 7; published 2018 December 26

Abstract

To characterize the substructures induced in protoplanetary disks by the interaction between stars in multiple systems, we study the 1.25 mm continuum and the ^{12}CO(J = 2–1) spectral line emission of the triple systems HT Lup and AS 205, at scales of ≈5 au, as part of the "Disk Substructures at High Angular Resolution Project" (DSHARP). In the continuum emission, we find two symmetric spiral arms in the disk around AS 205 N, with a pitch angle of 14°, while the southern component AS 205 S, itself a spectroscopic binary, is surrounded by a compact inner disk and a bright ring at a radius of 34 au. The ^{12}CO line exhibits clear signatures of tidal interactions, with spiral arms, extended arc-like emission, and high velocity gas, possible evidence of a recent close encounter between the disks in the AS 205 system, as these features are predicted by hydrodynamic simulations of flyby encounters. In the HT Lup system, we detect continuum emission from all three components. The primary disk, HT Lup A, also shows a two-armed symmetric spiral structure with a pitch angle of 4°, while HT Lup B and C, located at 25 and 434 au in projected separation from HT Lup A, are barely resolved with ∼5 and ∼10 au in diameter, respectively. The gas kinematics for the closest pair indicates a different sense of rotation for each disk, which could be explained by either a counter rotation of the two disks in different, close to parallel, planes, or by a projection effect of these disks with a close to 90° misalignment between them.

Key words: binaries (including multiple): close – dust, extinction – protoplanetary disks – techniques: high angular resolution

1. Introduction

In the early stages of star formation, the conservation of angular momentum through the gravitational collapse leads to the formation of a gas and dust disk around the young forming star; it is here where planetary systems may form. Given that most stars live or appear to have been formed in binary or multiple systems (Raghavan et al. 2010; Duchêne & Kraus 2013), it is expected that companions or close encounters will modify the disks in multiple stellar systems, when compared to disks around single, isolated stars.

Nonetheless, planets have been detected around single stars in multiple systems (e.g., Eggenberger et al. 2007; Chauvin et al. 2011), mostly at separations larger than a few tens of astronomical units, although this might be an effect of selection biases (Winn & Fabrycky 2015). Circumbinary planets have also been found (Doyle et al. 2011) sometimes in systems with more than one planet (Kepler-47, Kostov et al. 2013). However, Wang et al. (2014) find that planets should be 4.5 ± 3.2 and 2.6 ± 1.0 times less frequent in a multiple system (compared to single star systems), when a stellar companion is at a distance of 10 and 100 au, respectively (see also Kraus et al. 2016).

Over the last few years, the detection and characterization of dust and gas structures in disks at high angular resolution have been helping us to understand the processes involved in the evolution of young stars and the formation of planetary systems. Millimeter images that trace dust emission have shown large azimuthal asymmetries (e.g., van der Marel et al. 2013), spirals (e.g., Pérez et al. 2016), and bright/dark rings (e.g., ALMA Partnership et al. 2015), the latter appear to be the most common substructure in Class II disks (Andrews et al. 2018; Huang et al. 2018b). These features are often interpreted as signposts of planet–disk interactions (e.g., Zhu et al. 2011).

While multiplicity is high among young stars (e.g., ∼0.7 in Class II/III stars, ∼0.6 in Class 0 objects, Kraus et al. 2011; Tobin et al. 2016b), most observational studies at high angular resolution have so far focused on single stellar systems, and it is not clear how common such disk substructures are in multiple systems. Over the last two decades, a few multiple systems have been studied with sufficient angular resolution to resolve their components separately at radio wavelengths (Jensen et al. 1996; Jensen & Akeson 2003; Harris et al. 2012), and thanks to ALMA capabilities these detections have become more common over the last few years (e.g., Akeson & Jensen 2014; Jensen & Akeson 2014; Brinch et al. 2016; Tobin et al. 2016a). Misalignments between the disk rotation axis and the binaries' orbit (Williams et al. 2014; Fernández-López et al. 2017), as well

as tidal stripping and extended emission (Cabrit et al. 2006; Salyk et al. 2014; Rodriguez et al. 2018) have been detected in some of them. However, none of the previous observations reached the high spatial resolution required to study the substructure of disks in multiple systems. For example, spiral arms are expected to be triggered in the presence of one or multiple companions (Goldreich & Tremaine 1979; Tanaka et al. 2002), and could potentially be detected in the dust continuum emission at millimeter wavelengths. However, until today, most objects with known spiral-like structures in dust continuum emission (Pérez et al. 2016; Boehler et al. 2018; Dong et al. 2018) or gas emission (e.g., Tang et al. 2017) do not host any known stellar companion (an exception is HD 142527, Biller et al. 2012; Christiaens et al. 2014, 2018). This suggests that in these cases, the observed spirals might originate from other mechanisms, such as gravitational instabilities (Mayer et al. 2004; Lodato & Rice 2004), shadowing in the disk (Montesinos et al. 2016), or alternatively, that the possible companion(s) have not yet been detected.

The present work is the first step toward the detection and characterization of disk substructures, with high angular resolution observations (∼5 au) of multiple systems, which will help us understand how stellar interactions affect the evolution of gas and dust in protoplanetary disks. We present the first analysis of two young multiple systems, HT Lup and AS 205, observed as part of our ALMA Large Program "DSHARP: Disk Substructures at High Angular Resolution Project" (Andrews et al. 2018). In Section 2, we present the targets. In Section 3, we briefly describe the observations and specific calibration and imaging procedures. In Section 4, we present our analysis and modeling of these new data, which we further discuss in Section 5. Finally, we conclude and summarize our results in Section 6.

2. Targets

2.1. AS 205

AS 205 is a multiple stellar system located at a distance of 127 ± 2 pc (Gaia Collaboration et al. 2018) in the ρ-Ophiuchi star-forming region. The northern and southern components (from now on, AS 205 N and AS 205 S) have been detected at a projected separation of 1.″3 with near-infrared imaging (e.g., Ghez et al. 1993; Reipurth & Zinnecker 1993; McCabe et al. 2006), and imaged in 1.3 mm continuum and different CO molecular line observations (Andrews & Williams 2007; Salyk et al. 2014). The brightest of these sources at millimeter wavelengths is AS 205 N, a K5 pre-main-sequence star of about 0.5 Myr of age, with a mass of $0.87^{+0.15}_{-0.1}\,M_{\odot}$ (Eisner et al. 2005; Andrews et al. 2018) and a mass accretion rate of $4 \times 10^{-8}\,M_{\odot}\,\mathrm{yr}^{-1}$ (Andrews et al. 2009; Eisner et al. 2015). It shows multiple molecular emission lines in radio and midinfrared wavelengths (e.g., Öberg et al. 2011; Salyk et al. 2014), including water vapor lines (e.g., Salyk et al. 2008; Pontoppidan et al. 2010) and organics (Mandell et al. 2012). AS 205 S is itself a spectroscopic binary, with K7 and M0 spectral types and masses of 0.74 and 0.54 $M_{\odot}$ (Eisner et al. 2005).

Strong departure from Keplerian motion is detected in different molecular lines in this system and an extended emission is found around the disks that is unlikely to arise from envelope emission or from a large reservoir of mass that is being accreted by these disks (Salyk et al. 2014). Instead, it might be due to a combination of disks winds and perturbations produced by the binary interaction. Given that the synthesized beam could barely separate the N and S components (beam size ≈0.″7), only the large-scale features of this system could be identified.

The distances to each source in the AS 205 system used here were calculated from *Gaia* DR2 (Gaia Collaboration et al. 2018). However, we found a difference of almost 30 pc between AS 205 N and AS 205 S from their *Gaia* parallaxes (7.817 ± 0.098 and 6.376 ± 0.185 mas, respectively). As will be shown in Section 4, we are able to resolve the gas flow between the N and S components, previously detected in Salyk et al. (2014), and therefore conclude that the distance between disks must allow such an interaction. Since AS 205 S is an unresolved spectroscopic binary, Gaia DR2 did not account for the binary motion when calculating its parallax, which is calculated from the photocenter of each detected source (Lindegren et al. 2018). Because of this, in the following we consider the distance to AS 205 N as being the same for both northern and southern sources.

2.2. HT Lup

HT Lup is a triple stellar system located at a distance of 154 ± 2 pc (Gaia Collaboration et al. 2018) in the Lupus star-forming region, with an age of ≈0.8 Myr (Andrews et al. 2018). Its three components, hereafter referred to as HT Lup A, B, and C, have been identified through near-infrared imaging (Ghez et al. 1997; Correia et al. 2006) and interferometry (Anthonioz et al. 2015), with separations of ∼0.″1 between A and B, and ∼3″ between AB and C. Both B and C companions have lower luminosities than the primary, estimated to be 15% and 9.5% of that of HT Lup A (Anthonioz et al. 2015).

An extended nebulosity that resembles an arc-like structure is observed in the far-infrared with Herschel photometry (Cieza et al. 2013; Bustamante et al. 2015), while cloud contamination is also found in optical spectra (Herczeg & Hillenbrand 2014). At millimeter wavelengths, the HT Lup system has been observed by ALMA in continuum at 890 μm and 1.3 mm, and in CO molecular lines (Tazzari et al. 2017; Ansdell et al. 2018). All previous observations reach an angular resolution on the order of 0.″1, unable to resolve the closest companion, nor the individual disk structure and gas dynamics.

We estimate the distances for HT Lup A and C from *Gaia* DR2 (Gaia Collaboration et al. 2018), with the distance to C (154 ± 3 pc) being consistent with the A component at the 1σ level, showing that their proximity in the sky is not a projection effect.

3. Observations

The data sets presented here are part of DSHARP (Andrews et al. 2018). For AS 205, we also include band 6 archival data from ALMA Cycle 0 (Project number `2011.0.00531.S`), that were presented in Salyk et al. (2014), where the CO line was also observed. A detailed description of the data acquisition and calibration can be found in Andrews et al. (2018).

An identification of the peak position of HT Lup A was required in order to align astrometrically the different observations, following the procedure in Andrews et al. (2018). However, HT Lup A and B components can only be resolved using the long-baseline data sets, therefore, the peak location of HT Lup A could not be identified in the shortest baselines data sets. Given that HT Lup C was 2.″8 apart and isolated, we used its position as an alignment reference, before starting the self-calibration process.

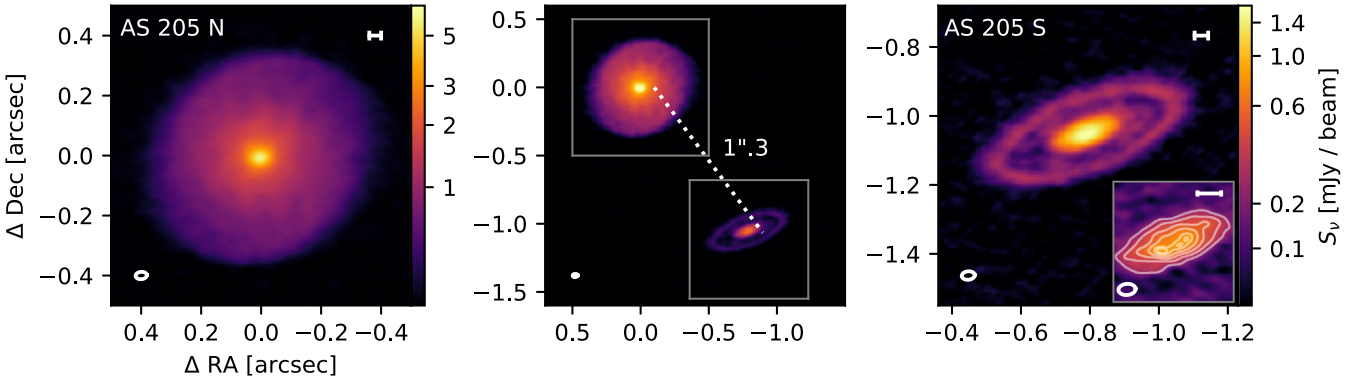

Figure 1. Continuum brightness distribution in the AS 205 system. The central panel indicates the separation between the two disks on the sky, while the left/right panels show AS 205 N/AS 205 S, respectively. An inset on the lower right corner of the AS 205 S panel presents a zoom to its inner disk, with observations imaged with different imaging parameters that provide higher spatial resolution (see the text). The coordinates have their origin in the continuum peak of AS 205 N. The beam size is 37 × 24 mas (4.7 × 3.0 au), as shown in the lower left corner of each panel, except for the inset in the AS 205 S panel, with a beam size of 29 × 16 mas (3.7 × 2.0 au). In this inset, the contour levels correspond to 10, 15, 20, 25, 30, and 32σ, where σ is the image rms. A scale of 5 au is indicated by the horizontal bar in the upper right corner on the AS 205 N and S panels. An arcsinh stretch is used for the color scale.

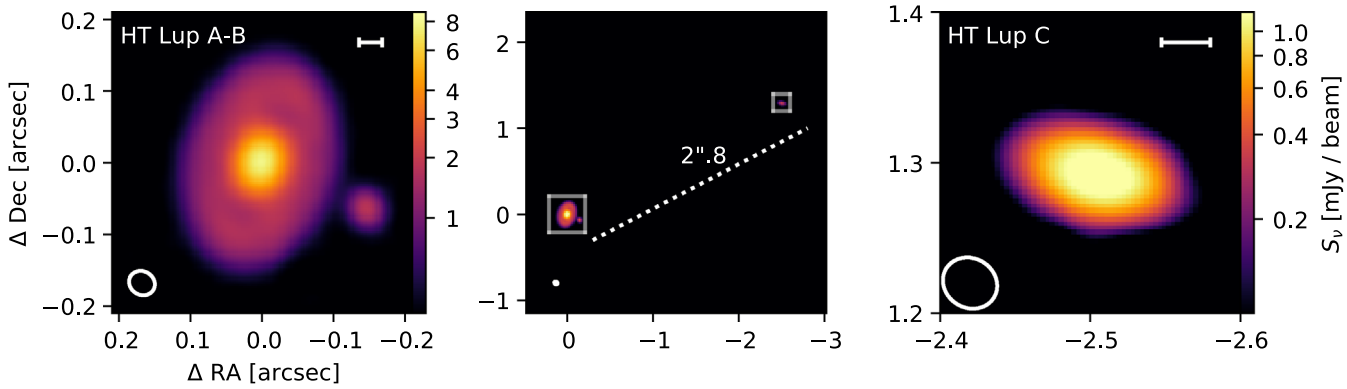

Figure 2. Continuum brightness distribution in the HT Lup system. The central panel shows the separation between the three disks on the sky, while the left/right panels show HT Lup A-B/HT Lup C, respectively. The coordinates have their origin in the continuum peak flux of HT Lup A. The beam size is 32 × 37 mas, as shown in the lower left of each panel, and a scale of 5 au is indicated by the horizontal bar in the upper right corner. An arcsinh stretch is used for the color scale.

The final images are centered at (J2000) R.A. = $16^h\,11^m\,31\overset{s}{.}352$, decl. = $-18^d\,38^m\,26\overset{s}{.}233$ for AS 205, and for HT Lup the center is at R.A. = $15^h\,45^m\,12\overset{s}{.}847$, decl. = $-34^d\,17^m\,31\overset{s}{.}01$.

After self-calibration, we generated continuum images using the `tclean` task in CASA 5.1 (McMullin et al. 2007). For AS 205 we chose a robust parameter of 0.5, resulting in the 1.25 mm continuum images displayed in Figure 1, with a beam size of 37 × 24 mas (4.7 × 3.0 au). In addition, we also created an image with uvtaper of 40 × 0 mas and PA = 90° (measured from north to east) to circularize the beam and increase the signal-to-noise ratio (S/N) in extended emission, which was only used to study the substructure of AS 205 N, while an image with robust = −0.5 was used to take a look into the compact central emission of AS 205 S. The first continuum image has an S/N of 390 with an rms of 16 μJy/beam, the second has an S/N of 645 with an rms of 18 μJy/beam, and the third has an S/N of 136 and an rms of 26 μJy/beam.

While most of the CO maps in our survey are imaged with beams of ≈100 mas, for the disks around these multiple systems we synthesized beams with smaller sizes, in order to distinguish structures inside the most compact sources. Channel maps from CO in AS 205 were generated using a robust parameter of 1. to obtain a beam of 90 × 67 mas (≈8.5 au at best), which led to an rms of 1.42 mJy/beam per velocity channel, and a peak S/N of 35.3. The AS 205 channel maps are presented in Figure 9 of the Appendix.

For HT Lup continuum we chose a robust parameter of 0.5, and the resulting 1.3 mm images are displayed in Figure 2, with a beam size of 37 × 32 mas (5.7 × 4.9 au), an rms of 14.1 μJy/beam and a peak S/N of 585. In order to obtain the cleanest possible CO map, we excluded baselines smaller than 150 m, thus, decreasing the sensitivity to scales larger than 2″, emphasizing compact emission. The CO images used a robust parameter of 1.5, and we additionally applied a *uv*-tapering of 20 × 5 mas with PA = 150°, resulting in a beam of 53 × 50 mas (≈8 au). The rms of this spectral cube is 1.2 mJy/beam per velocity channel, with a peak S/N of 10.5. The HT Lup channel maps are presented in Figure 10 of the Appendix.

4. Results

4.1. Continuum Emission in the AS 205 System

In the continuum emission, the AS 205 system resolves into two disks whose peaks are separated by 1.″313, or 168 au in projected separation (central panel, Figure 1), along a position angle (PA) of 217°. The AS 205 N disk is not azimuthally symmetric; instead, a spiral-like pattern with low contrast is observed (left panel, Figure 1). The AS 205 S disk is fainter and

Table 1
Results of 2D Gaussian Fit to Each Continuum Disk

Source	R.A. (J2000)	Decl. (J2000)	Major Axis[a]	Minor Axis[a]	i	PA
AS 205 N[b]	16:11:31.352	−18:38:26.34	$0\farcs414 \pm 0.006$	$0\farcs388 \pm 0.006$	$20\fdg1 \pm 3\fdg3$	$114\fdg0 \pm 11\fdg8$
AS 205 S	16:11:31.296	−18:38:27.29	$0\farcs185 \pm 0.006$	$0\farcs077 \pm 0.003$	$66\fdg3 \pm 1\fdg7$	$109\fdg6 \pm 1\fdg8$
HT Lup A	15:45:12.847	−34:17:31.01	$0\farcs156 \pm 0.010$	$0\farcs104 \pm 0.007$	$48\fdg1 \pm 4\fdg5$	$166\fdg1 \pm 6°$
HT Lup B	15:45:12.835	−34:17:31.08	$0\farcs032 \pm 0.001$	$0\farcs022 \pm 0.002$	$44\fdg9 \pm 4\fdg9$	$8\fdg3 \pm 7\fdg5$
HT Lup C	15:45:12.645	−34:17:29.72	$0\farcs059 \pm 0.001$	$0\farcs025 \pm 0.001$	$65\fdg5 \pm 0\fdg9$	$78\fdg8 \pm 0\fdg8$

Notes.
[a] Deconvolved Gaussian values.
[b] For this target the fit was done on the short-baseline images only, to avoid including substructure in the 2D Gaussian fit.

smaller in angular size than AS 205 N, and it exhibits a narrow ring around an inner disk (right panel, Figure 1), where a cavity is observed when imaged at high angular resolution (see the inset in the right panel, Figure 1).

In other DSHARP targets with spiral features (e.g., Elias 2–27 or IM Lup, Huang et al. 2018a) there are symmetric substructures (bright or dark rings) that can be used to constrain the geometry of the disk. However, the lack of symmetric features in AS 205 N implies that we have to use a different method to constrain the disk inclination (i) and PA. Given that the two sources are well separated in the sky, we fitted a 2D Gaussian model to each disk using the CASA task `imfit`. For AS205 N, we used the continuum image generated while excluding the longest baseline data set, with a beam size of 270×227 mas, to avoid including any asymmetric feature. The best-fit values are given in Table 1. With the values of i and PA derived, we find that the angular momentum vectors of the disks are misaligned by either 46° or 94° (see equation in, e.g., Jensen & Akeson 2014), depending on whether the two disks share the same near side (the disk side closer to the observer).

4.1.1. Spirals in AS 205 North

We calculate the azimuthally averaged radial profile of the continuum emission, considering i and PA as constrained above, and using the peak of emission as center (which coincides with the peak of the 2D Gaussian fitted within 3 mas, about one-tenth of the beam size). After subtracting this radial profile from the continuum image, a clear spiral structure is revealed, as shown in Figure 3. These spiral features can be traced between ∼20 and 55 au, beyond this radius the intensity of the continuum disk goes below the 3σ level. To trace the northwest (NW) and southeast (SE) spiral arms, we define a set of discrete points that correspond to the peak of emission along the radial direction, spaced by 10° in azimuth (which corresponds to one synthesized beam at ∼30 au) and identified where the disk emission is above 3σ.

To characterize each spiral, we consider models of a logarithmic spiral defined as:

$$r = r_0 \cdot \exp(b\theta) \quad (1)$$

and of an Archimedean spiral, defined as:

$$r = r_0 + b\theta, \quad (2)$$

where θ is the azimuthal angle, r_0 is the radius when the angle is 0, and b relates to the pitch angle μ of the spiral. For the logarithmic spiral, the pitch angle is constant along all radii and it is calculated as $\mu = \arctan(1/b)$, while for the Archimedean model, the pitch angle depends on the radius as $\mu = b/r$.

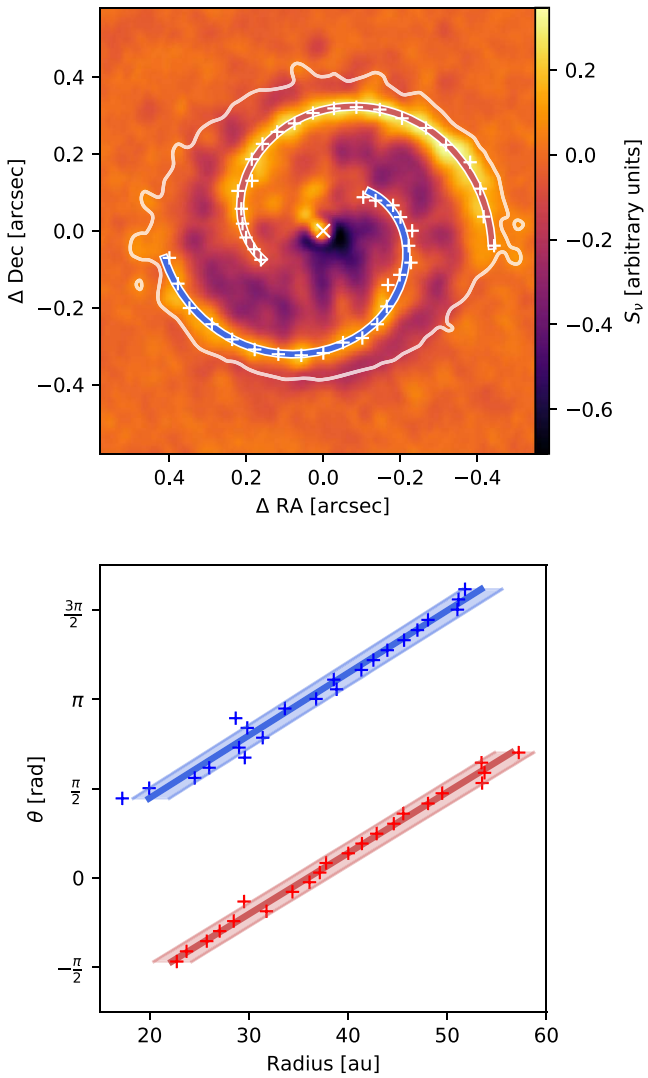

Figure 3. Top panel: continuum emission of AS 205 N after subtraction of its azimuthally averaged radial profile. The plus symbols mark the location of the maximum of emission along the spiral arms, with the best-fit archimedean model in red (NW) and blue (SE) lines. The contour level surrounding the disk marks the 5σ level of the original image (before subtraction of the radial profile). The center of the spirals was fixed, and its position is marked with a white cross. Bottom panel: deprojected spiral wake, with colors as in the top panel. The best-fit model is shown with a solid line, and the shaded region represents the 1σ uncertainties of our best fit.

The NW and SW spirals are assumed to share the same center (located at the peak of emission), while the spiral parameters r_0 and b are fitted separately for each arm to test if

Table 2
Best-fit and 1σ Uncertainties from the Fit of the Spiral Shape in AS 205 N

Parameter	Log.	Arch.
$r_{0,\mathrm{NW}}$	$26.1^{+1.3}_{-1.1}$ au	$36.0^{+2.0}_{-1.8}$ au
$r_{0,\mathrm{SE}}$	$11.9^{+0.7}_{-0.6}$ au	$7.2^{+2.1}_{-1.6}$ au
b_{NW}	$0.244^{+0.005}_{-0.006}$	$9.32^{+0.23}_{-0.15}$
b_{SE}	$0.246^{+0.005}_{-0.006}$	$9.10^{+0.16}_{-0.23}$
μ_{NW}	$13\overset{\circ}{.}9^{+0.3}_{-0.3}$	$15\overset{\circ}{.}3$ at 35 au
μ_{SE}	$13\overset{\circ}{.}7^{+0.3}_{-0.3}$	$14\overset{\circ}{.}9$ at 35 au
i	$15\overset{\circ}{.}1^{+1.9}_{-3.2}$	$14\overset{\circ}{.}3^{+1.3}_{-5.3}$
PA	$-9\overset{\circ}{.}1^{+10.7}_{-8.7}$	$59\overset{\circ}{.}6^{+13.0}_{-10.3}$

Note. The pitch angles μ are calculated from b. For the Archimedean model, μ is calculated at 35 au.

these are symmetric or not. We also include the observed inclination (i) and PA as free parameters, assuming both spirals share the same geometry. Therefore, we have six free parameters ($r_{0,\mathrm{NW}}$, $r_{0,\mathrm{SE}}$, b_{NW}, b_{SE}, i, and PA). To fit the spiral prescriptions above, we use an MCMC routine based on `emcee` (Foreman-Mackey et al. 2013). A flat prior probability was used for all parameters. For each fit, we use 250 walkers with two consecutive burning stages of 1000 and 500 steps, and then 1500 steps to sample the parameter space. The results of the logarithmic and Archimedean spiral model fit are given in Table 2. We note that the reduced χ^2 in the Archimedean spiral model is a factor of 1.5 better than in the logarithmic model. Figure 3 shows the best-fit Archimedean spiral and the location of emission maxima in the image (top panel) and in polar coordinates (bottom panel).

We note that we tested a model that allows for an offset of the spirals with respect to the center (two additional free parameters). The model finds an offset that is smaller than $\approx$3 au, with the NW and SE spirals' pitch angle differing from but consistent with each other within 1σ. Since the reduced χ^2 is comparable to the model with fixed center, we chose to use the latter for simplicity.

We calculate the contrast between the spiral and inter-spiral region, by comparing the intensity of each arm with the lower 5% intensity of a ring at the same radial distance. We found the arms to be of low contrast, with only factors of 1.4 and 1.3 (median value) between the spiral and the inter-spiral region, for the NW and SE spirals, respectively. The contrast between the NW and SE spirals is small, $\approx$1.1 on average.

4.1.2. A Ring in AS 205 South

The disk around AS 205 S is also well resolved in the continuum. The peak of emission for this component is 2.4 mJy/beam (185σ), which is only 29% of the AS 205 N peak, the mean surface brightness of the ring is around 57.6 μJy/beam (32σ).

At equally spaced intervals of 18°, i.e., points are roughly spaced by one synthesized beam, we search for the position of the maximum emission along the ring. The points were then fitted with an ellipse using an MCMC routine based on `emcee` (Foreman-Mackey et al. 2013), leaving the center, major axis, minor axis, and PA free to vary. The walkers and steps used are similar to the spiral fit. The points selected along the ring and the best-fit model are shown in Figure 4, while the best-fit parameters are given in Table 3.

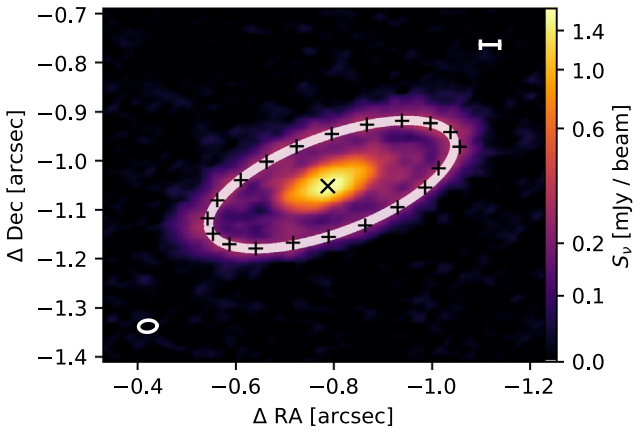

Figure 4. Fit of an ellipse to the AS 205 S ring in the outer disk. The plus symbols mark the maximum emission along the ring, while the white line shows the best fit. At the center, the black cross marks the best-fit center of the ellipse. The beam is given in the bottom-left corner, and a 5 au scale bar is in the upper-right corner for comparison.

Table 3
Results from the MCMC Search for Best-fit Parameters of a Ring in AS 205 S

Parameter	Value.
Δx	$-0.42^{+0.22}_{-0.3}$ au
Δy	$0.23^{+0.17}_{-0.18}$ au
major axis	$33.8^{+0.3}_{-0.4}$
minor axis	12.4 ± 0.2 au
i	$68\overset{\circ}{.}4^{+0.5}_{-0.7}$
PA	$110\overset{\circ}{.}6^{+0.5}_{-0.4}$

Note. Errors correspond to 1σ. Note that the major axis corresponds to the radius of the ring.

From the fit, we find that the ring center matches the peak flux within 3 mas ($\sim$1/10 of the beam size), and that the ring inclination and PA are also in good agreement with the values obtained with the 2D Gaussian fit to the image.

4.2. Gas Emission in the AS 205 System

We detect CO emission from this system from $v = -7.6$ to $+12.0\,\mathrm{km\,s^{-1}}$, with little cloud contamination over this velocity range. Figure 5 shows the integrated intensity (moment 0) while Figure 6 also presents the intensity-weighted velocity field (moment 1) computed from the CO data cube, clipping at 3σ and including only channels with detected emission (see Figure 5.10 of Andrews et al. 2018 for all channel maps, and Figure 9 in the Appendix for channels of interest). Evidence of tidal interaction is clearly seen in the gas tracer, with CO emission between the two continuum sources on channels between $v = 3.25$ and $5.35\,\mathrm{km\,s^{-1}}$. The AS 205 N disk shows a butterfly pattern characteristic of Keplerian motion around the central star, which allow us to estimate its systemic velocity to be $\approx$4.5 $\mathrm{km\,s^{-1}}$ (emission above 3σ is observed from $v = -0.1$ to $+8.5\,\mathrm{km\,s^{-1}}$). However, this Keplerian pattern only holds inside the region where the continuum emission is above 3σ, at approximately 60 au from disk center. Outside this region, we observe extended emission and several arc-like structures that extend to the outskirts of the disk (at most at 410 au, $\approx 3\overset{''}{.}2$).

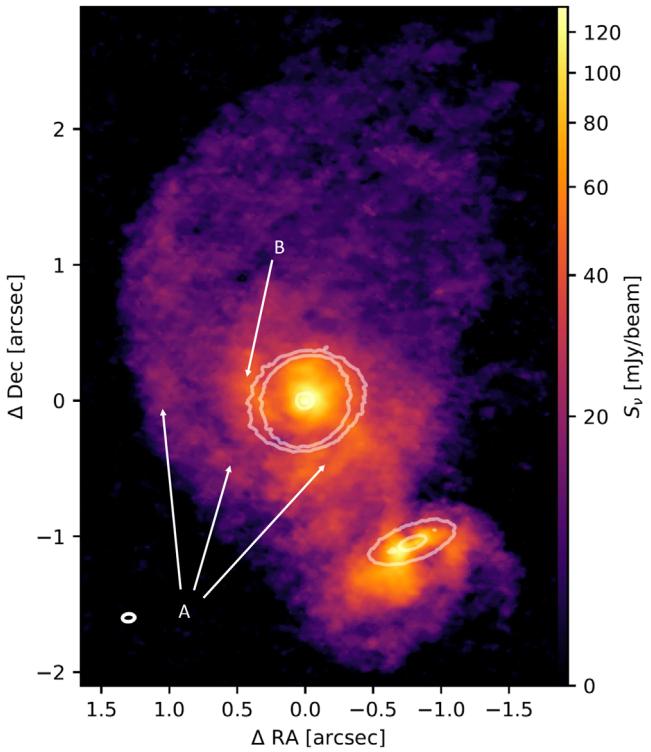

Figure 5. Integrated emission map (moment zero) of the CO spectral cube in the AS 205 system. The two main arcs of emission in AS 205 N are labeled A and B (see Figure 9). The contour levels represent 5, 25, and 300σ of the continuum emission, for comparison.

On the north and south sides of the continuum disk, there are arc-like structures in CO that resemble spiral arms. The most prominent arc (that starts in the west and turns clockwise to the south and then east, labeled A in Figure 5), roughly coincides with the NW continuum spiral, as is shown with the best-fit model for this spiral in dotted lines in Figure 6 (left panels). However, further out than ∼80 au (∼0.″5) the arc does not have the same opening angle as the NW continuum spiral. In the moment 1 map from Figure 6, the trace of arc A appears to have constant velocity (∼4.5 km s^{-1}) over its extension outside of the continuum disk. In the moment 0 map, another spiral-like structure can be distinguished toward the east (labeled B in Figure 5), but this feature is not colocated with the best-fit SE continuum spiral. Furthermore, arc B is not clearly observed across channels maps, and no velocity structure that corresponds to this arc can be distinguished in the moment 1 map either.

As can be seen in the moment 1 map of the CO in AS 205 S (Figure 6, rightmost panel), the southern component shows disk rotation, but quite perturbed. First, due to its high inclination ($\sin i \approx 0.9$) the inner disk emission can be seen at high velocities from $v = -7.6$ to $+12.0$ km s^{-1}, which is about a factor of two wider velocity range than for AS 205 N. Non-Keplerian motion is seen in the southeast of AS 205 S over all channels. At velocity channels near 4.3 km s^{-1}, the gas emission appears as a broad arc toward the south, better appreciated as the bright emission in the south of the AS 205 S moment 0 map.

4.3. Continuum Emission in the HT Lup System

Three components are detected in this system, Figure 2 shows the 1.3 mm continuum map where we are able to spatially resolve the dust continuum emission around the closest pair: HT Lup A and B. The angular separations between HT Lup A and B, and HT Lup A and C are 0.″161 and 2.″82, respectively, which corresponds to projected separations of 25 and 434 au. We fitted a 2D Gaussian using `imfit` in CASA to derive inclinations and PAs for all disks, listed in Table 1. From these values, and following the same procedure used in AS 205, we estimate the misalignment between the angular momentum of the disks to be either 91° or 164° for HT Lup A and B, and 76° or 108° for A and C.

4.3.1. Spirals in HT Lup A

HT Lup A is the brightest and more extended disk in the system, with emission above 3σ detected up to 33 au (≈0.″21) from the center. Computing an average radial profile of emission on this disk is difficult due to the presence of the companion at close distance (HT Lup B). Thus, to subtract the overall disk emission and enhance the nonaxisymmetric features in the disk, we use an unsharped masking technique. We first convolve the image with a Gaussian of 66 mas FWHM and then subtract it from the original continuum image, multiplying by a weighting factor of 0.95. We chose these unsharp masking parameters as they better enhanced the low-contrast spiral features (convolution with larger Gaussians smooths out the disk emission excessively, smaller Gaussians do not smooth out the nonsymmetric features and these end up being subtracted instead of enhanced). The resulting image, shown in Figure 7, reveals an underlying spiral structure. We trace the arms as in AS 205 N, finding the maxima along radial directions separated by 8°. The spirals extend from ≈16.5 to ≈19 au in radius, and each arm covers an azimuthal extent of ≈100°.

Following the procedure in Section 4.1.1, we fit a logarithmic and Archimedean spiral model, with the best-fit parameters presented in Table 4. The results show spirals with low pitch angles that are quite symmetric; however, they are so compact that possible asymmetries might remain unresolved by our observations. The inclination and PA are in agreement with the values obtained from Gaussian fitting.

4.3.2. Companions: HT Lup B and HT Lup C

HT Lup B appears barely spatially resolved, its peak intensity (1.85 mJy/beam, 131σ) is 23% of the HT Lup A peak intensity. From the 2D Gaussian fitting we obtain a deconvolved FWHM size of 31 ± 2 mas, corresponding to a disk size of ∼5 au.

The farthest companion, HT Lup C, is the faintest source in the system, with a peak intensity of 1.6 mJy/beam (20% of the peak of HT Lup A) and a total integrated flux of 3.48 mJy. From the 2D Gaussian fit, we measure a deconvolved size of 59 ± 1 mas, which corresponds to a disk size of ∼9 au.

4.4. Gas Emission in the HT Lup System

A map of the CO emission was obtained following the DSHARP procedure (Andrews et al. 2018). However, the CO was found to be highly contaminated by extended cloud emission and foreground absorption near the systemic velocity ($v_{\rm sys} \approx 5.5$ km s^{-1}), at the level of completely erasing the signal from the disks between 3.75 and 4.8 km s^{-1}. (for all channel maps, see Figure 5.1 of Andrews et al. 2018, while channels of interest are in Figure 9 in the Appendix). For

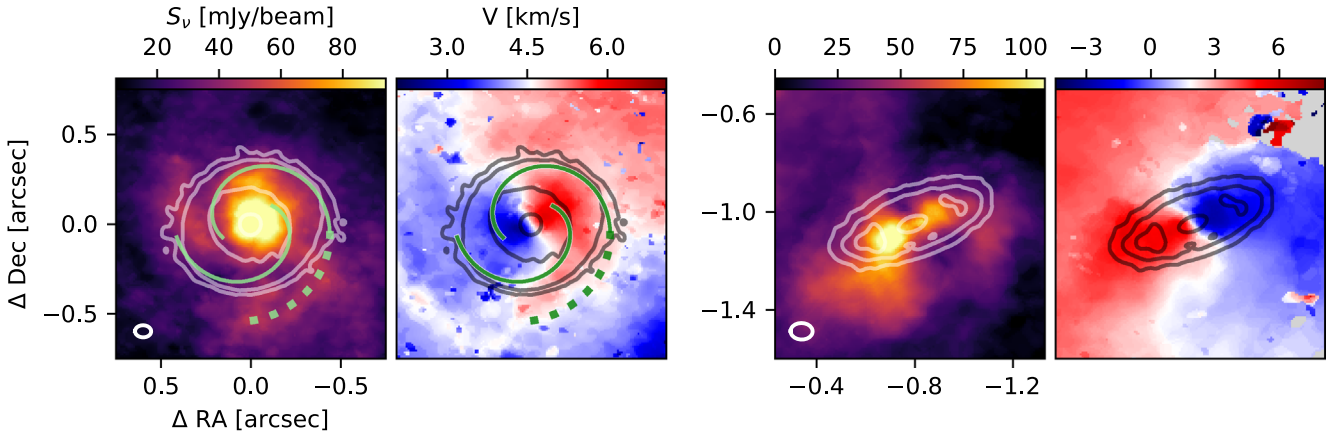

Figure 6. Moment 0 and moment 1 images of the CO emission in AS 205 N (left panels) and AS 205 S (right panels). The beam size (57 × 54 mas) is shown at the bottom left corner of each moment 0 image. For AS 205 N, we draw in green the best archimedean fit to continuum spirals, and the NW spiral is extended as a dashed line for comparison. The contour lines mark the 5σ, 25σ, 120σ, and 300σ levels in the continuum image.

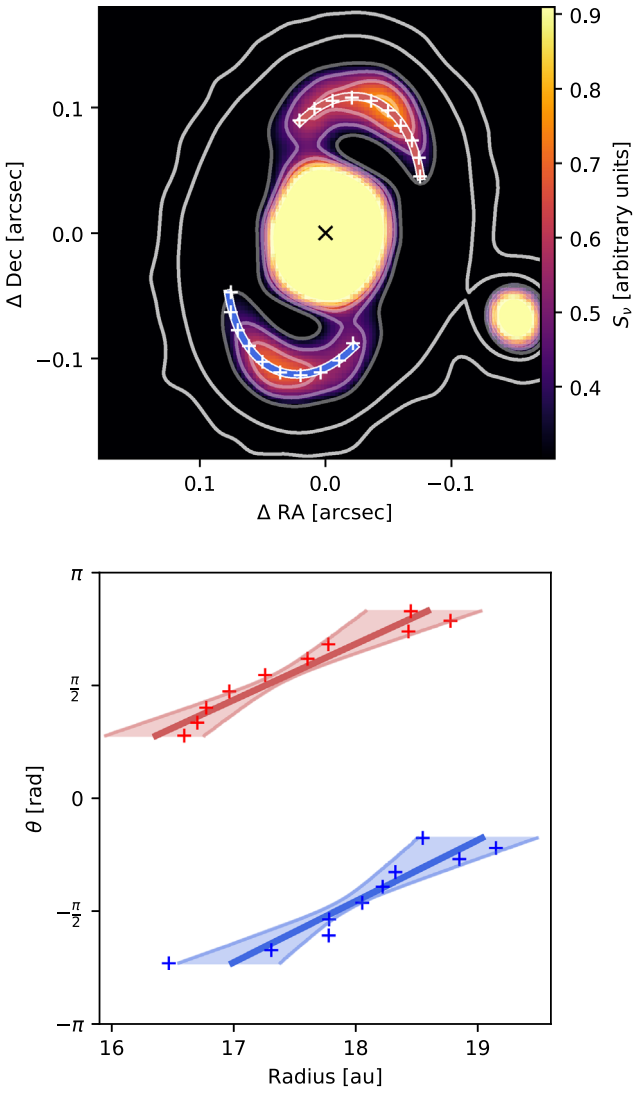

Figure 7. Top panel: the HT Lup A/HT Lup B unsharp-masked continuum image. The plus symbols mark the maximum emission along the spirals. The solid colored line represents the best Archimedean spiral models. Solid outer lines show contour levels at 5σ and 28σ of the original continuum image. The color scale was chosen to emphasize spiral arms. Bottom panel: deprojected spiral wake, with colors as in the top panel. The best-fit model is shown as a solid line, and the shaded region represents the 1σ uncertainties of our best fit.

Table 4
Best-fit and 1σ Uncertainties from the Fit of the Spiral Shape in HT Lup A

Parameter	Log.	Arch.
$r_{0,N}$	$15.4^{+1.9}_{-1.8}$ au	15.3 ± 0.8 au
$r_{0,S}$	$19.7^{+0.8}_{-0.7}$ au	$19.7^{+0.7}_{-0.8}$ au
b_N	$0.073^{+0.025}_{-0.03}$	$1.28^{+0.5}_{-0.51}$
b_S	$0.064^{+0.025}_{-0.03}$	$1.17^{+0.5}_{-0.51}$
μ_N	$4.^\circ15^{+1.4}_{-1.7}$	4.°1 at 18 au
μ_S	$3.^\circ69^{+1.4}_{-1.7}$	3.°7 at 18 au
i	$52.^\circ2^{+0.6}_{-0.9}$	$53.^\circ0^{+0.6}_{-0.7}$
PA	$14.^\circ3^{+2.3}_{-1.8}$	$14.^\circ2^{+2.2}_{-2.1}$

Note. The pitch angles μ are calculated from b. For the Archimedean model, μ is calculated at 18 au.

HT Lup A, blueshifted emission is seen in the north, while redshifted emission appears in the south. The opposite is observed for HT Lup B. This is better seen in the first moment map of CO emission, presented in Figure 8, in which the disks appear to be counter-rotating. HT Lup C is also observed in the CO, with emission detected from $v = 2.7$ to 9.7 km s^{-1}, extending ∼0.″2 along its major axis, which lies horizontally as expected from its continuum shape.

5. Discussion

5.1. Ruling Out Chance Alignment

Given that the AS 205 components have different parallaxes as measured by *Gaia* DR2 (resulting in a difference of almost 30 pc in distance, see Section 2.1), and that for the HT Lup system there are no constraints on the distance to source B (while the A and C components have consistent *Gaia* parallaxes), one could argue that the observed vicinity of these pairs is due to chance alignment. In the case of AS 205, an interaction between AS 205 N and S is observed in CO emission in these observations, as well as in earlier works (Salyk et al. 2014).

In the case of HT Lup, with speckle imaging, Ghez et al. (1997) find that the angular separation between HT Lup A and B is 0.″107 ± 0.″007 in 1997, while Correia et al. (2006) measure a separation of 0.″126 ± 0.″001 with data from 2004, using Very Large Telescope observations. In this work, we constrain a

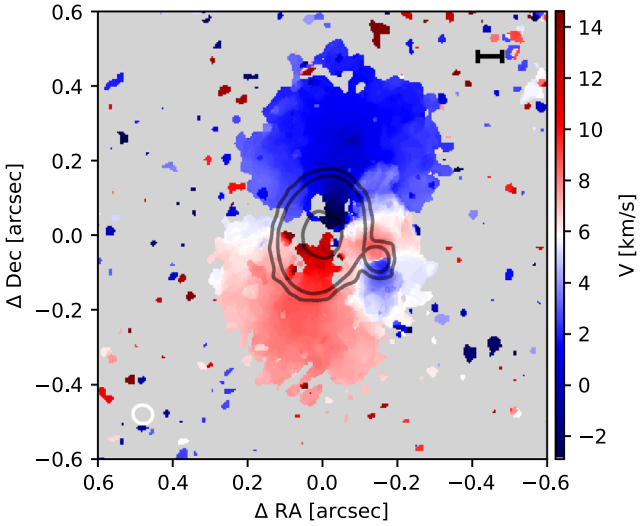

Figure 8. Moment 1 of the CO emission in the region of HT Lup A and HT Lup B. The beam size is $0\farcs053 \times 0\farcs049$, presented in the bottom-left corner of the image, as well as a 10 au scale bar at the upper-right corner. The contour lines mark the 5σ, 28σ, and 150σ levels of the continuum image, for comparison.

separation of $0\farcs161 \pm 0\farcs003$ with data from 2017. Thus, in the span of ∼20 yr, HT Lup A and B have changed their separation by ∼50 mas. Given the proper motion of HT Lup A ($\mu_{\rm R.A.} = -13.63 \pm 0.13$ mas yr^{-1}, $\mu_{\rm Decl.} = -21.61 \pm 0.08$ mas yr^{-1}, Gaia Collaboration et al. 2018), if the pair was aligned by chance, then their separation should have changed by ∼500 mas over this timespan, an order of magnitude larger than that measured. We therefore conclude that most likely, the HT Lup A and B stars as well as the AS 205 N and S components are not aligned by chance.

5.2. Substructures in the Dust Continuum Emission

The high resolution observations of the multiple systems HT Lup and AS 205 have allowed us, for the first time, to directly constrain the type of substructures present in protoplanetary disks that have an ongoing interaction. In the following, we discuss the different substructures found in gas and dust tracers, and compare with other systems or numerical simulations.

5.2.1. Spiral Arms

The spiral arms observed in the primary components of these systems are quite different from each other, and only AS 205 N looks similar to the spirals observed in single systems from the DSHARP sample (e.g., WaOph 6 and IM Lup, Huang et al. 2018a).

The HT Lup A disk is quite compact (32 au radius) and the radial extent of the spirals is only ∼4 au (about 10% of the disk size). However, to describe the maxima of emission in the unsharped masking image, our modeling prefers a spiral over a ring for these substructures in HT Lup A: solutions with 0° pitch angle (i.e., a ring) are excluded at the 2.5σ level. But even at this high angular resolution it is difficult to resolve the substructure in HT Lup A. A bar-like emission is observed connecting the two spiral arms with the inner disk, something that is not described by our models (Figure 7).

On the other hand, the AS 205 N disk has spiral features that are well resolved by our observations. These spirals appear to be better described by an Archimedean model than a logarithmic one, in terms of the reduced χ^2 of each model, and since the former model better captures the spiral shape at both spiral ends. Thus, a variable pitch angle is preferred over a constant pitch angle to describe the AS 205 N spirals.

Interestingly, HT Lup A and AS 205 N show spiral features in the dust over a smaller range of radii and azimuthal angles than the other DSHARP spiral detections in Huang et al. (2018a). In fact, the radial extents of the spirals (≈36 au for AS 205 N and ≈4 au for HT Lup A) are smaller than the spirals observed in Elias 27, IM Lup, and Wa Oph 6, which range in radial extent from ≈50 to ≈180 au. This difference in size could be explained by the truncation of the outer disk predicted in binary disk simulations or simulations of disks that have been involved in flyby encounters (Clarke & Pringle 1993; Breslau et al. 2014; Winter et al. 2018) This will be further discussed in Section 5.3.

5.2.2. Axisymmetric Substructures

The bright rings and dark annulus observed in the single systems with spirals from DSHARP (Huang et al. 2018a) are not observed in the disks of the multiples systems presented here. The lack of additional substructures may be explained by the small disk sizes: in the single systems with spiral arms, the gaps/rings usually show up at radial distances $\gtrsim$75 au, while our largest disk (AS 205 N) appears truncated at $\lesssim$60 au. If ring-like substructures are formed from pressure traps induced by planets, the lack of this substructure in HT Lup A and AS 205 N disks might suggest that stellar encounters and close binary companions inhibit planet formation, through disk truncation and material stripping, in agreement with the lower frequency of planet detections around binaries compared to single star systems (Wang et al. 2014).

Only AS 205 S displays a prominent outer ring at 34 au, with a bright inner disk out to ∼20 au, with both substructures separated by a gap. When imaged with a robust value of −0.5, we obtain an image of the disk with a smaller beam size (16 mas, 2 au resolution at best), in which the inner disk is no longer centrally peaked, and a cavity starts to be resolved (see Figure 1). This constrains the spectroscopic binary separation to be smaller than ∼2 au in the southern component of AS 205.

The unperturbed nature of the AS 205 S dust ring is puzzling. Assuming the spectroscopic binary has a total mass of 1.3 $M_\odot$ (Eisner et al. 2005), the orbital period at the ring location would be 173 yr. Close encounter simulations of star–disk interactions show that tidal stripping and arc-like features can be induced in timescales from a hundred to a few thousand years (e.g., RW Aurigae, Dai et al. 2015). Thus, if the AS 205 system had a flyby interaction (see Section 5.3) the ring at 34 au in AS205S has only had $\lesssim$10 orbits to recover its structure after the interaction. Most likely, the dynamical interaction could not have originated from a very close encounter, which would have disrupted or severely affected this ring.

5.3. A Flyby in AS 205 System?

By analyzing the gas kinematics, disk rotation is identified in the N and S components of AS 205. However, we also observe non-Keplerian features such as the flow or bridge of material

between the disks, an extended arc-like emission (arc A) toward the north in AS 205 N, an asymmetric emission toward the southeast in AS 205 S, and a tilt/twist of the projected axis of rotation in AS 205 N and S (see moment 1 map of these object in Figure 6).

These features are quite similar to the ones observed in flyby interactions in parabolic-like orbits. For example, the 3D hydrodynamic flyby simulations from Dai et al. (2015) exhibit several of the non-Keplerian features present in the AS205 system, such as the gas bridge between the disks and the arc-like structure extending from the main component. Since for prograde encounters (i.e., when the interaction occurs in the same direction as the disk rotation) the material stripped and/or transferred from one disk to the other is more pronounced, rather than for retrograde encounters (Clarke & Pringle 1993; Dai et al. 2015), it seems that the prograde case is a closer match to our observations. In addition, an orthogonal or prograde noncoplanar encounter is expected to produce a warp in the disk (Clarke & Pringle 1993; Cuello et al. 2018), tilting and then twisting it, modifying the line of nodes, as observed in the velocity field of AS 205 N and S (moment 1 maps, Figure 6).

The truncated spatial extent of AS 205 N in the dust can also be explained by a prograde flyby interaction, which would strip off material from the main disk resulting in an outer disk radius that depends on the companion mass, the angle of interaction between disk plane and companion orbit, and the distance at periastron (Clarke & Pringle 1993). Further simulations and observations will help to better constrain these parameters.

5.4. Disk Misalignment in the HT Lup A-B Binary

In the close binary HT Lup A-B, we observe an apparent counter-rotation of their disks in Figure 8. Given the degeneracy in the estimate of the misalignment between the disks, two different cases can explain the observations:

1. The angular momentum vectors are misaligned by 91°, leaving the disks almost perpendicular to each other. If we assume that the spiral arms in HT Lup A are trailing (i.e., the disk rotation is counterclockwise), then the nearest side of the disk is in the east. For such a misalignment, assuming counterclockwise rotation, the nearest side in HT Lup B would then be in the west, and the observed counter-rotation of the two disks would merely be a projection effect. Since we do not observe features in the CO channel maps that indicate transfer of material, an obvious perturbation in the butterfly pattern, or disk truncation in gas, this configuration is only possible if their physical separation is large enough in our line of sight.
2. The angular momentum vectors are misaligned by 164°, with the disks close to parallel and counter-rotating. As the trailing spirals assumption implies that HT Lup A rotates counterclockwise, HT Lup B would in this case rotate clockwise, and its nearest side toward us would be its east side. As in the previous case, this would only be possible if the two disks are not in the same plane but instead, physically distant along our line of sight.

Misalignments have been previously identified in other multiple systems (Jensen & Akeson 2014; Williams et al. 2014; Brinch et al. 2016), but the separations of these systems are much larger (hundreds of astronomical units) than in HT Lup A-B. Bate (2018) presents hydrodynamical simulations that indicate that misaligned disks in binaries are possible, mainly due to fragmentation in turbulent environments and stellar capture. In addition, a complete flip of the disk orientation can occur due to gas accretion from the cloud with different angular momentum. These results show that, in principle, misalignments can arise in any direction depending on the cloud surroundings and environment where the disks are formed. A possible scenario for the formation of the HT Lup A-B system is an independent fragmentation of the binary components from the cloud, followed by a capture and subsequent orbital decay, leaving them close together and misaligned.

Future observations with high S/N in molecular lines, less contaminated from the cloud, and at similar or higher angular resolution, should be able to discern between the two scenarios, solving the degeneracy of disk orientation. A follow-up of the HT Lup B and HT Lup C orbital positions will be also needed to get a complete description of the heavy truncation, misalignments, and dynamics in the HT Lup system.

6. Conclusions

We present very high resolution (∼5 au scales) ALMA observations of the multiple stellar systems AS 205 and HT Lup, observed in band 6 (1.3 mm) as part of DSHARP (Andrews et al. 2018).

In the continuum emission, the AS 205 system resolves into two separate disks located at 168 au projected separation. The disk around AS 205 N shows two spiral arms extending from about 20 to 55 au in radius and over 180° in azimuthal angle. By fitting them with an Archimedean and logarithmic spiral models, we find these arms to have similar pitch angles, close to 14°; though, these are better described by the Archimedean model with a radially varying pitch angle. The southern component, AS 205 S, displays an inner disk and a bright ring at 34 au, with a gap between the inner disk and outer ring that is not devoid of continuum emission. The CO observations of AS 205 show extended emission in the form of arc-like structures, with non-Keplerian motions observed around both disks. We found evidence to support that these features were triggered by the binary interaction via a close encounter or flyby, which was also suggested by Salyk et al. (2014). In this scenario, the AS 205 system would have either a highly eccentric orbit between its components, or had a recent unbound interaction. Nevertheless, the regularity of the AS 205 S dust ring puts constrains over the proximity and timescale of this interaction, since the ring does not appear as perturbed as the gas.

For the first time at millimeter wavelengths, we resolve the two companions (B and C) in the HT Lup system, the closest one with a projected separation of 25 au from HT Lup A. HT Lup C is located at more than 400 au from HT Lup A-B. The disks around HT Lup B and C are the smallest objects in the DSHARP sample, with deconvolved sizes of ≈5 and ≈10 au, respectively. The HT Lup A disk is resolved and spiral structure is observed, which we constraint to be symmetric with a pitch angle close to 4°. However, the spirals are quite compact and appear to connect with the inner disk through a bar-like structure. Higher angular resolution might be needed in future observations to completely characterize this additional substructure. The kinematics of the CO emission in the closest binary, HT Lup A-B, shows an apparent counter-rotation of

their disks. Given the degeneracy in disk orientation, we find two possible explanations depending on the angle between their angular momentum vectors, which could either be a near to perpendicular relative orientation of their disks, in which case the counter-rotation would only be a projection effect, or alternatively, a close to parallel orientation of the disks with a physical counter-rotation that requires the disks to not be on the same plane.

The observations from DSHARP of multiple young stellar systems presented here, as well as future ALMA observations of gas and dust tracers at high angular resolution, are excellent laboratories to study dynamical interactions in multiple systems and to understand how this may affect the process of star and planet formation. This work is the first step toward a better understanding of how binary interactions and flybys affect a disk's structure, its evolution, and the efficiency of planet formation.

We are thankful to N. Cuello for insightful discussions. This paper makes use of ALMA data sets ADS/JAO.ALMA#2016.1.00484.L and ADS/JAO.ALMA#2011.0.00531.S. ALMA is a partnership of ESO (representing its member states), NSF (USA) and NINS (Japan), together with NRC (Canada), *MOST* and ASIAA (Taiwan), and KASI (Republic of Korea), in cooperation with the Republic of Chile. The Joint ALMA Observatory is operated by ESO, AUI/NRAO, and NAOJ. Powered@NLHPC: This research was partially supported by the supercomputing infrastructure of the NLHPC (ECM-02), Center for Mathematical Modeling CMM, Universidad de Chile. L.P. acknowledges support from CONICYT project Basal AFB-170002, from FCFM/U. de Chile Fondo de Instalación Académica, and from FONDECYT Iniciación project #11181068. M.B. acknowledges funding from ANR of France under contract number ANR-16-CE31-0013 (Planet Forming disks). Z.Z. and S.Z. acknowledges support from the National Aeronautics and Space Administration through the Astrophysics Theory Program with grant No. NNX17AK40G and Sloan Research Fellowship. Simulations are carried out with the support from the Texas Advanced Computing Center (TACC) at The University of Texas at Austin through XSEDE grant TG-AST130002. J.H. acknowledges support from the National Science Foundation Graduate Research Fellowship under grant No. DGE-1144152. S.A. and J.H. acknowledge funding support from the National Aeronautics and Space Administration under grant No. 17-XRP17_2-0012 issued through the Exoplanets Research Program. C.P.D. acknowledges support by the German Science Foundation (DFG) Research Unit FOR 2634, grants DU 414/22-1 and DU 414/23-1. A.I. acknowledges support from the National Aeronautics and Space Administration under grant No. NNX15AB06G issued through the Origins of Solar Systems program, and from the National Science Foundation under grant No. AST-1715719. V.V.G. and J.C acknowledge support from the National Aeronautics and Space Administration under grant No. 15XRP15_20140 issued through the Exoplanets Research Program. L.R. acknowledges support from the ngVLA Community Studies program, coordinated by the National Radio Astronomy Observatory, which is a facility of the National Science Foundation operated under cooperative agreement by Associated Universities, Inc.

Appendix

Here we present the spectral data cubes (channel maps) of AS 205 (Figure 9) and HT Lup (Figure 10).

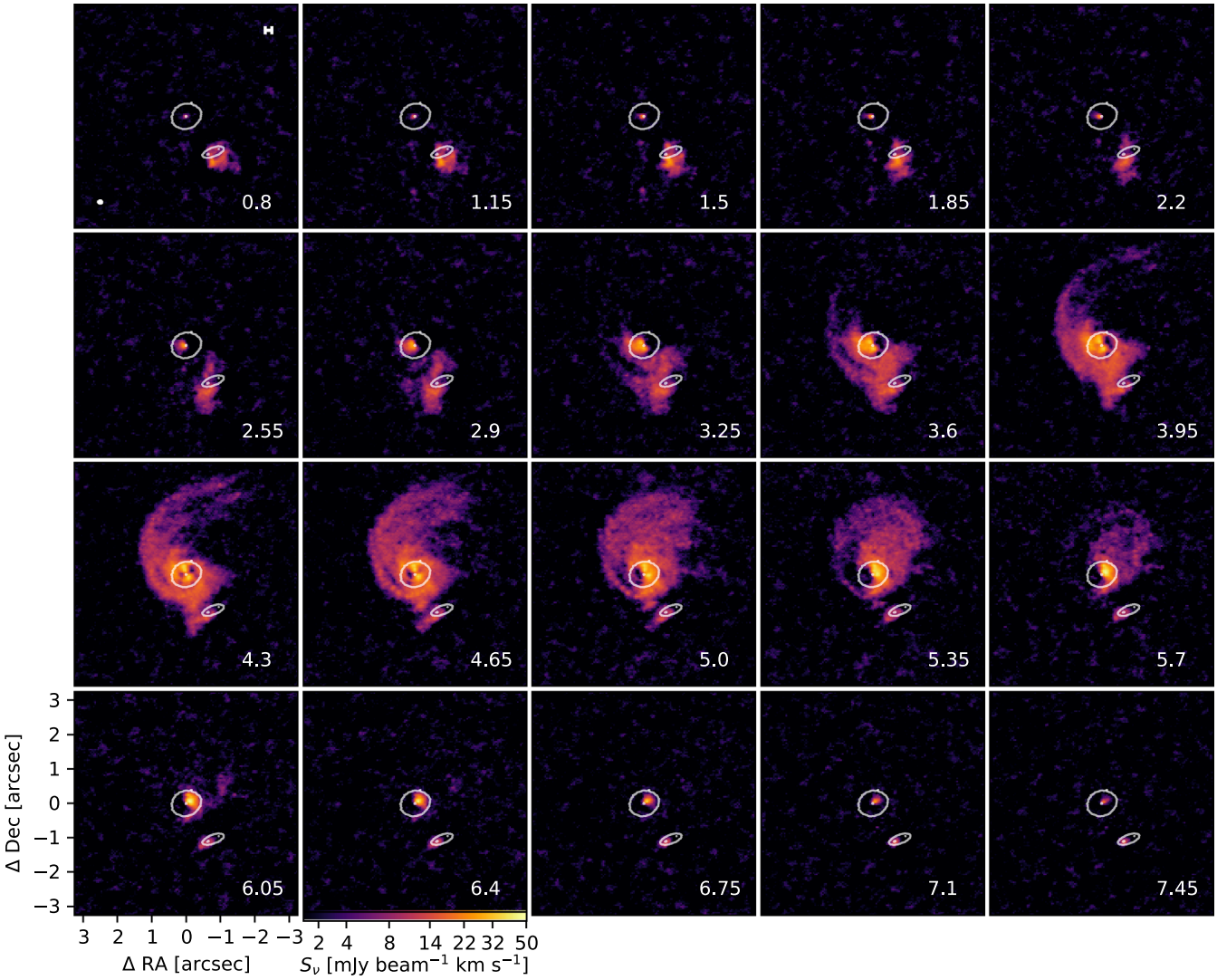

Figure 9. Channel maps of the CO emission in the AS 205 system. Each box is $7\farcs5$ wide and centered at the continuum luminosity peak of AS 205 N. The LSRK velocity is printed in the lower right corner of each frame, while the beam size and a 25 au scale bar are printed in the first image at the upper left frame. The contour levels correspond to 5σ and 300σ in continuum, for comparison.

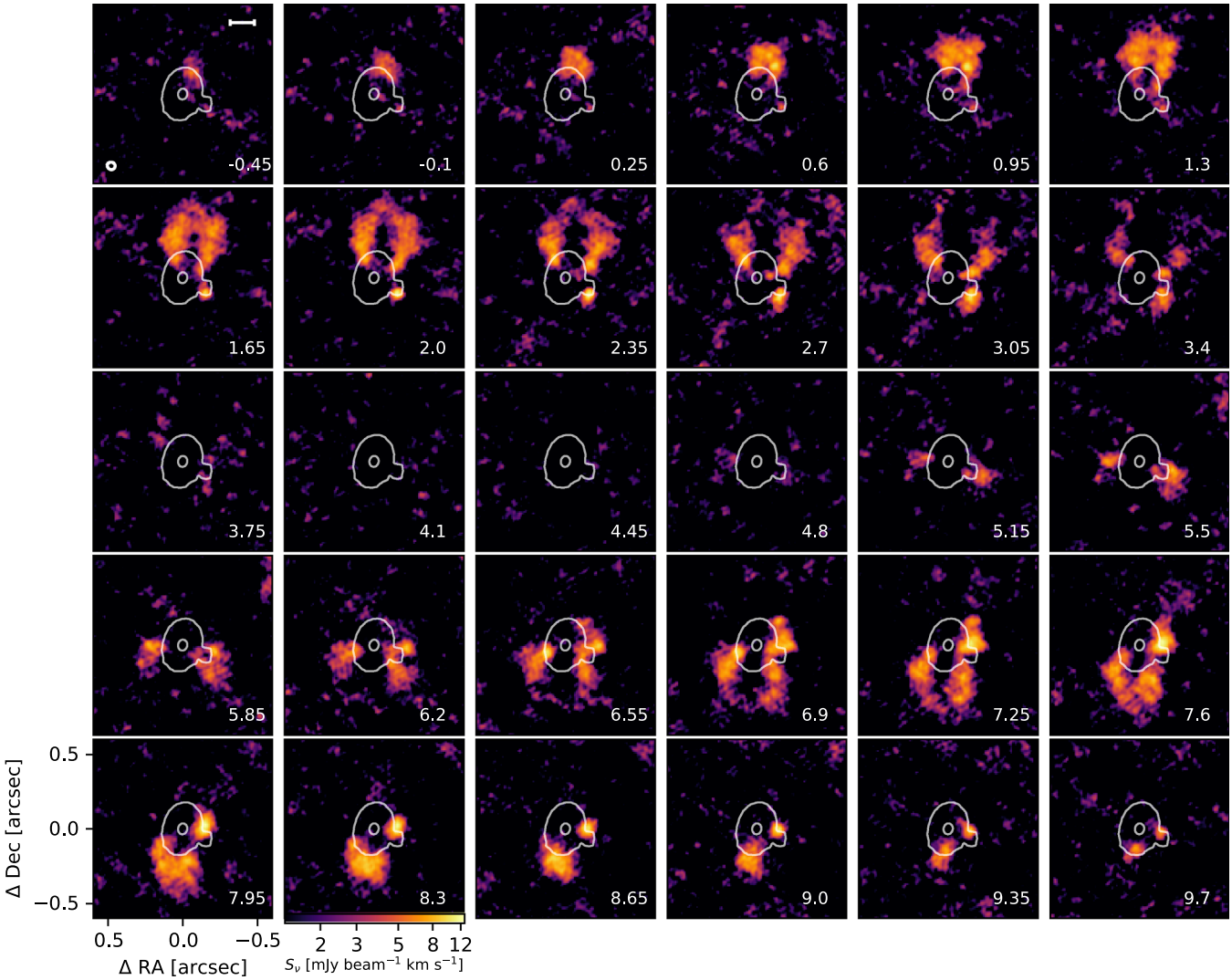

Figure 10. CO emission of HT Lup A/HT Lup B. Each square is 1.″2 per side and centered at the peak flux of HT Lup A in continuum. The LSRK velocity is printed in the lower right corner of each frame, while the beam size and a 25 au scale bar are printed in the first image in the upper left frame. The image was generated by removing all baselines with less than 150 m in length, losing sensitivity at scales larger than 2″. The contour levels correspond to 5σ and 300σ in the continuum image, for comparison.

ORCID iDs

Laura M. Pérez https://orcid.org/0000-0002-1199-9564
Myriam Benisty https://orcid.org/0000-0002-7695-7605
Zhaohuan Zhu https://orcid.org/0000-0003-3616-6822
Shangjia Zhang https://orcid.org/0000-0002-8537-9114
Jane Huang https://orcid.org/0000-0001-6947-6072
Sean M. Andrews https://orcid.org/0000-0003-2253-2270
Cornelis P. Dullemond https://orcid.org/0000-0002-7078-5910
Andrea Isella https://orcid.org/0000-0001-8061-2207
John M. Carpenter https://orcid.org/0000-0003-2251-0602
Viviana V. Guzmán https://orcid.org/0000-0003-4784-3040
David J. Wilner https://orcid.org/0000-0003-1526-7587

References

Akeson, R. L., & Jensen, E. L. N. 2014, ApJ, 784, 62
ALMA Partnership, Brogan, C. L., Pérez, L. M., et al. 2015, ApJL, 808, L3
Andrews, S. M., Huang, J., Pérez, L., et al. 2018, ApJL, 869, L41
Andrews, S. M., & Williams, J. P. 2007, ApJ, 659, 705
Andrews, S. M., Wilner, D. J., Hughes, A. M., Qi, C., & Dullemond, C. P. 2009, ApJ, 700, 1502
Ansdell, M., Williams, J. P., Trapman, L., et al. 2018, ApJ, 859, 21
Anthonioz, F., Ménard, F., Pinte, C., et al. 2015, A&A, 574, A41
Bate, M. R. 2018, MNRAS, 475, 5618
Biller, B., Lacour, S., Juhász, A., et al. 2012, ApJL, 753, L38
Boehler, Y., Ricci, L., Weaver, E., et al. 2018, ApJ, 853, 162
Breslau, A., Steinhausen, M., Vincke, K., & Pfalzner, S. 2014, A&A, 565, A130
Brinch, C., Jørgensen, J. K., Hogerheijde, M. R., Nelson, R. P., & Gressel, O. 2016, ApJL, 830, L16
Bustamante, I., Merín, B., Ribas, Á., et al. 2015, A&A, 578, A23
Cabrit, S., Pety, J., Pesenti, N., & Dougados, C. 2006, A&A, 452, 897
Chauvin, G., Beust, H., Lagrange, A. M., & Eggenberger, A. 2011, A&A, 528, A8
Christiaens, V., Casassus, S., Absil, O., et al. 2018, A&A, 617, A37
Christiaens, V., Casassus, S., Perez, S., van der Plas, G., & Ménard, F. 2014, ApJL, 785, L12
Cieza, L. A., Olofsson, J., Harvey, P. M., et al. 2013, ApJ, 762, 100
Clarke, C. J., & Pringle, J. E. 1993, MNRAS, 261, 190
Correia, S., Zinnecker, H., Ratzka, T., & Sterzik, M. F. 2006, A&A, 459, 909
Cuello, N., Dipierro, G., Mentiplay, D., et al. 2018, MNRAS, sty3325 (https://academic.oup.com/mnras/advance-article-abstract/doi/10.1093/mnras/sty3325/5234243?redirectedFrom=fulltext)

Dai, F., Facchini, S., Clarke, C. J., & Haworth, T. J. 2015, MNRAS, 449, 1996
Dong, R., Liu, S.-y., Eisner, J., et al. 2018, ApJ, 860, 124
Doyle, L. R., Carter, J. A., Fabrycky, D. C., et al. 2011, Sci, 333, 1602
Duchêne, G., & Kraus, A. 2013, ARA&A, 51, 269
Eggenberger, A., Udry, S., Chauvin, G., et al. 2007, A&A, 474, 273
Eisner, J. A., Hillenbrand, L. A., White, R. J., Akeson, R. L., & Sargent, A. I. 2005, ApJ, 623, 952
Eisner, J. A., Rieke, G. H., Rieke, M. J., et al. 2015, MNRAS, 447, 202
Fernández-López, M., Zapata, L. A., & Gabbasov, R. 2017, ApJ, 845, 10
Foreman-Mackey, D., Hogg, D. W., Lang, D., & Goodman, J. 2013, PASP, 125, 306
Gaia Collaboration, Brown, A. G. A., Vallenari, A., et al. 2018, A&A, 616, A1
Ghez, A. M., Neugebauer, G., & Matthews, K. 1993, AJ, 106, 2005
Ghez, A. M., White, R. J., & Simon, M. 1997, ApJ, 490, 353
Goldreich, P., & Tremaine, S. 1979, ApJ, 233, 857
Harris, R. J., Andrews, S. M., Wilner, D. J., & Kraus, A. L. 2012, ApJ, 751, 115
Herczeg, G. J., & Hillenbrand, L. A. 2014, ApJ, 786, 97
Huang, J., Andrews, S. M., Cleeves, L. I., et al. 2018b, ApJ, 852, 122
Huang, J., Andrews, S. M., Pérez, L. M., et al. 2018a, ApJL, 869, L43
Jensen, E. L. N., & Akeson, R. 2014, Natur, 511, 567
Jensen, E. L. N., & Akeson, R. L. 2003, ApJ, 584, 875
Jensen, E. L. N., Koerner, D. W., & Mathieu, R. D. 1996, AJ, 111, 2431
Kostov, V. B., McCullough, P. R., Hinse, T. C., et al. 2013, ApJ, 770, 52
Kraus, A. L., Ireland, M. J., Huber, D., Mann, A. W., & Dupuy, T. J. 2016, AJ, 152, 8
Kraus, A. L., Ireland, M. J., Martinache, F., & Hillenbrand, L. A. 2011, ApJ, 731, 8
Lindegren, L., Hernández, J., Bombrun, A., et al. 2018, A&A, 616, A2
Lodato, G., & Rice, W. K. M. 2004, MNRAS, 351, 630
Mandell, A. M., Bast, J., van Dishoeck, E. F., et al. 2012, ApJ, 747, 92
Mayer, L., Wadsley, J, Quinn, T., & Stadel, J 2004, in ASP Conf. Ser. 321, Extrasolar Planets: Today and Tomorrow, ed. J Beaulieu, A. Lecavelier Des Etangs, & C. Terquem (San Francisco, CA: ASP), 290
McCabe, C., Ghez, A. M., Prato, L., et al. 2006, ApJ, 636, 932
McMullin, J. P., Waters, B., Schiebel, D., Young, W., & Golap, K. 2007, in ASP Conf. Ser. 376, Astronomical Data Analysis Software and Systems XVI, ed. R. A. Shaw, F. Hill, & D. J. Bell (San Francisco, CA: ASP), 127
Montesinos, M., Perez, S., Casassus, S., et al. 2016, ApJL, 823, L8
Öberg, K. I., Qi, C., Fogel, J. K. J., et al. 2011, ApJ, 734, 98
Pérez, L. M., Carpenter, J. M., Andrews, S. M., et al. 2016, Sci, 353, 1519
Pontoppidan, K. M., Salyk, C., Blake, G. A., & Käufl, H. U. 2010, ApJL, 722, L173
Raghavan, D., McAlister, H. A., Henry, T. J., et al. 2010, ApJS, 190, 1
Reipurth, B., & Zinnecker, H. 1993, A&A, 278, 81
Rodriguez, J. E., Loomis, R., Cabrit, S., et al. 2018, ApJ, 859, 150
Salyk, C., Pontoppidan, K., Corder, S., et al. 2014, ApJ, 792, 68
Salyk, C., Pontoppidan, K. M., Blake, G. A., et al. 2008, ApJL, 676, L49
Tanaka, H., Takeuchi, T., & Ward, W. R. 2002, ApJ, 565, 1257
Tang, Y.-W., Guilloteau, S., Dutrey, A., et al. 2017, ApJ, 840, 32
Tazzari, M., Testi, L., Natta, A., et al. 2017, A&A, 606, A88
Tobin, J. J., Kratter, K. M., Persson, M. V., et al. 2016a, Natur, 538, 483
Tobin, J. J., Looney, L. W., Li, Z.-Y., et al. 2016b, ApJ, 818, 73
van der Marel, N., van Dishoeck, E. F., Bruderer, S., et al. 2013, Sci, 340, 1199
Wang, J., Fischer, D. A., Xie, J.-W., & Ciardi, D. R. 2014, ApJ, 791, 111
Williams, J. P., Mann, R. K., Di Francesco, J., et al. 2014, ApJ, 796, 120
Winn, J. N., & Fabrycky, D. C. 2015, ARA&A, 53, 409
Winter, A. J., Clarke, C. J., Rosotti, G., et al. 2018, MNRAS, 478, 2700
Zhu, Z., Nelson, R. P., Hartmann, L., Espaillat, C., & Calvet, N. 2011 ApJ, 729, 47